Short-range order and strong interplay between local and itinerant magnetism in $GeFe_3N$

Tinghai Zhang,[1] Yantao Cao,[2,3,4] Bo Zhang,[5,6] Hanjie Guo,[2,*] Liang Qiao,[1] Fashen Li,[1] and Zhiwei Li[1,†]

[1]*School of Physical Science and Technology, Lanzhou University, Lanzhou 730000, Gansu, China*

[2]*Songshan Lake Materials Laboratory, Dongguan 523808, Guangdong, China*

[3]*Institute of Physics, Chinese Academy of Sciences, Beijing 100190, China*

[4]*School of Physical Sciences, University of Chinese Academy of Sciences, Beijing 100049, China*

[5]*State Key Laboratory of Low-Dimensional Quantum Physics and Department of Physics, Tsinghua University, Beijing 100084, China*

[6]*Frontier Science Center for Quantum Information, Tsinghua University, Beijing 100084, China*

(Received 23 July 2024; revised 24 October 2024; accepted 20 November 2024; published 11 December 2024)

Here, we report on comprehensive structural, magnetic, specific heat, resistivity, and microscopic ^{57}Fe Mössbauer spectroscopy investigations of the $GeFe_3N$ compound. The experimental results indicate that the ground state of $GeFe_3N$ is short-range ordered ferromagnetic (FM) state, where the FM clusters are embedded in the paramagnetic background. Our density functional theory (DFT) calculations have revealed possible orbital order for the FeII site, and the strong interplay between the local moments for the FeI site and the itinerant moments for the FeII site may be responsible for the observed short-range FM order. We believe that these results are crucial for a complete understanding of the peculiar magnetic properties reported for $GeFe_3N$ and may also shed light on the understanding of the complex relationships between the structure and magnetism in related compounds.

DOI: 10.1103/PhysRevB.110.224419

I. INTRODUCTION

The interactions between magnetic moments, either localized or itinerant, may lead to diverse ground states including not only the most well-known ferromagnetism and antiferromagnetism [1] but also other interesting states ranging from spin liquids [2] to skyrmion lattices [3] and d^0 magnetism [4]. By investigating the vast majority of magnetic materials, great achievements have been made in understanding the local and itinerant moment magnetism. However, for real materials that lie somewhere between the local-itinerant moment extremes, a theoretical description of the complex intermediate moment picture is currently lacking [5]. Identifying the nature of magnetism, local or itinerant, and unraveling the interplay between them within heavy fermion materials might shed light on the nontrivial properties of strongly correlated systems such as spin- and charge-density waves [6–10].

Recently, the ternary iron-nitride compounds stand out to be an interesting playground for investigating the relationships between magnetism and subtle structural distortions in iron-rich phases. These compounds with a common formula of AFe_3N (A = Ge, Ca, Al, etc.) often crystallize in the cubic ABO_3 perovskite-type structure with space group $Pm\bar{3}m$ [11–14]. The perovskite structure can be described as a network of corner-sharing BO_6 octahedra with the A site cation in between. Moreover, the perovskite structure often distorts from the cubic structure by rotations and tilts of the BO_6 octahedra [15,16], such as the Ge containing compound $GeFe_3N$ with space group $I4/mcm$ [17] [see Fig. 1(a)]. In this structure, the Ge and N atoms are located at the Wyckoff sites 4b (0, 0.5, 0.25) and 4c (0, 0, 0), respectively, while the Fe atoms occupy two nonequivalent sites labeled as FeI at 4a (0, 0, 0.25) and FeII at 8h (0.19, 0.69, 0). This means that the FeII atoms exhibit a rotation with respect to the FeI atoms, which leads to a deviation from the diagonal position of (0.25 0.75 0) [see Fig. 1(b)]. Most interestingly, Tsumuraya *et al.* have predicted very different magnetic behaviors for the two Fe sites by first-principles density functional theory (DFT) calculations, namely, local and itinerant magnetism for the FeI and FeII sites, respectively [18]. The competition and interplay between the local moments and the itinerant moments may be responsible for the frustrated ferromagnetic (FM) state and the critical behavior observed in $GeFe_3N$ compound [17].

To better understand the different magnetic behaviors at the two Fe sites, we have performed local probe Mössbauer spectroscopy measurements on polycrystalline samples of $GeFe_3N$. Together with comprehensive macroscopic measurements and DFT calculations, we have established the short-range ordered FM ground state of $GeFe_3N$. We further reveal the strong interplay between the local magnetic moments at the FeI site and the itinerant magnetic moments from the FeII site and the possible orbital order at the FeII site from our DFT calculations.

II. EXPERIMENTS AND RESULTS

Polycrystalline samples of $GeFe_3N$ were synthesized by the conventional solid-state reaction method [17]. The phase purity was confirmed by x-ray diffraction measurement performed on a Rigaku x-ray diffractometer with Cu Kα

*Contact author: hjguo@sslab.org.cn

†Contact author: zweili@lzu.edu.cn

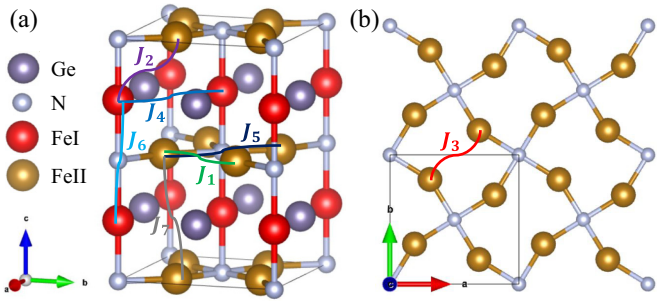

FIG. 1. (a) Crystal structure of $GeFe_3N$ in the conventional unit cell. (b) The top view of the FeII layer showing the rotation of the FeII atoms away from the diagonal position (0.25 0.75 0). The atomic positions are optimized using the CASTEP code with Perdew-Burke-Ernzerhof (PBE)_ functional as described in the text. The first seven pairwise exchange interaction paths are indicated in the figure. This figure was drawn using the software VESTA [19].

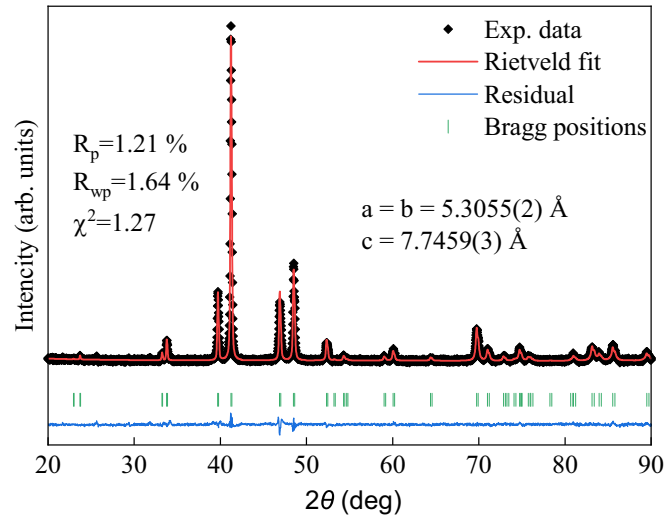

FIG. 2. Rietveld refinement of the powder x-ray diffraction pattern of the $GeFe_3N$ polycrystals collected at room temperature.

radiation. FULLPROF SUITE [20] was used for crystal structure refinement. The sample composition was checked with an energy dispersive spectrometer (EDS) equipped within a scanning electron microscope (SEM), and the determined Ge/Fe ratio amounts to 0.326(15), being very close to the nominal composition.

DC magnetic susceptibility was measured using the vibrating sample magnetometer (VSM) option of the Physical Property Measurement System (PPMS, Quantum Design). AC magnetic susceptibility between 20 and 120 K was measured using the ACMS-II options of the PPMS. A driven field of 5 Oe in amplitude was used. Specific heat and resistivity measurements were carried out on the same PPMS.

Mössbauer spectroscopy measurements were performed in transmission geometry with a conventional spectrometer working in constant acceleration mode. A 50-mCi γ-ray source of ^{57}Co embedded in Rh matrix vibrating at room temperature was used. The drive velocity was calibrated using sodium nitroprusside (SNP) and the isomer shifts quoted in this paper are relative to that of the α-Fe at room temperature. All the measured Mössbauer spectra were analyzed using the software MOSSWINN [21].

A. Structure

Figure 2 shows the x-ray diffraction (XRD) pattern of our $GeFe_3N$ polycrystalline sample. All peaks can be indexed with the tetragonal structure with space group $I4/mcm$. The XRD pattern was refined by the FULLPROF SUITE [20]. The determined lattice constants amount to $a = b = 5.3055(2)$ Å and $c = 7.7459(3)$ Å. These values are consistent with reported lattice parameters $a = 5.3053$ Å and $c = 7.7632$ Å for $GeFe_3N$ [17]. On the other hand, the $Fe_3GeN_{0.51}$ sample with less nitrogen content has smaller values of $a = 5.231$ Å and $c = 7.658$ Å [22]. The refined atomic positions are listed in Table I. Since the lattice parameters depend sensitively on the nitrogen content, these results confirm nicely the stoichiometry of the nitrogen content in our sample. The site positions for the FeII atoms from XRD refinement and DFT optimization amount to (0.2 0.7 0) and (0.19 0.69 0), respectively, as listed in Table I; both are smaller than the reported value of (0.23 0.73 0) for $Fe_3GeN_{0.51}$ [22], which points to a larger rotation of the FeII atoms away from the diagonal position (0.25 0.75 0) as shown in Fig. 1(b).

B. DC susceptibility

The temperature-dependent magnetization $M(T)$ (left axis) and inverse susceptibility $\chi^{-1}(T)$ (right axis) curves of $GeFe_3N$ measured under an external field of $H = 0.1$ T are shown in Fig. 3(a). With decreasing temperature, both zero-field-cooled (ZFC) and field-cooled (FC) curves start to increase steeply below ~95 K, indicating the onset of the FM-like ordering (we will label this FM-like transition as T_c, following earlier reports [17], despite its short-range nature that we will discuss later). However, unlike typical FM materials, the magnetization curve measured in the FC mode never saturates even to the lowest temperature, ~2 K. As will be shown later, this is attributed to the short-range nature of the FM order developed below T_c. The FM-like transition is also evident from the isothermal magnetization loops $M(H)$ measured at various temperatures as shown in Fig. 3(b).

Above T_c, the complex nonlinear $\chi^{-1}(T)$ curve indicates the breakdown of the Curie-Weiss behavior. Nevertheless, the solid line in Fig. 3(a) is a tentative fit to the $\chi^{-1}(T)$ data using

TABLE I. Crystal structural parameters of $GeFe_3N$ refined from our XRD data at room temperature in space group $I4/mcm$ with the lattice parameters $a = 5.3055(2)$ Å and $c = 7.7459(3)$ Å. The DFT optimized lattice parameters with PBE functional are $a = 5.21126$ Å and $c = 7.74688$ Å.

Atom	Site	x/a	y/b	z/c
Ge	4b	0.0	1/2	1/4
N	4c	0.0	0.0	0.0
FeI	4a	0.0	0.0	1/4
FeII	8h	0.20095(16)	0.70095(16)	0.0
DFT(PBE)	Optimized	Results		
FeII	8h	0.19028	0.69028	0.0

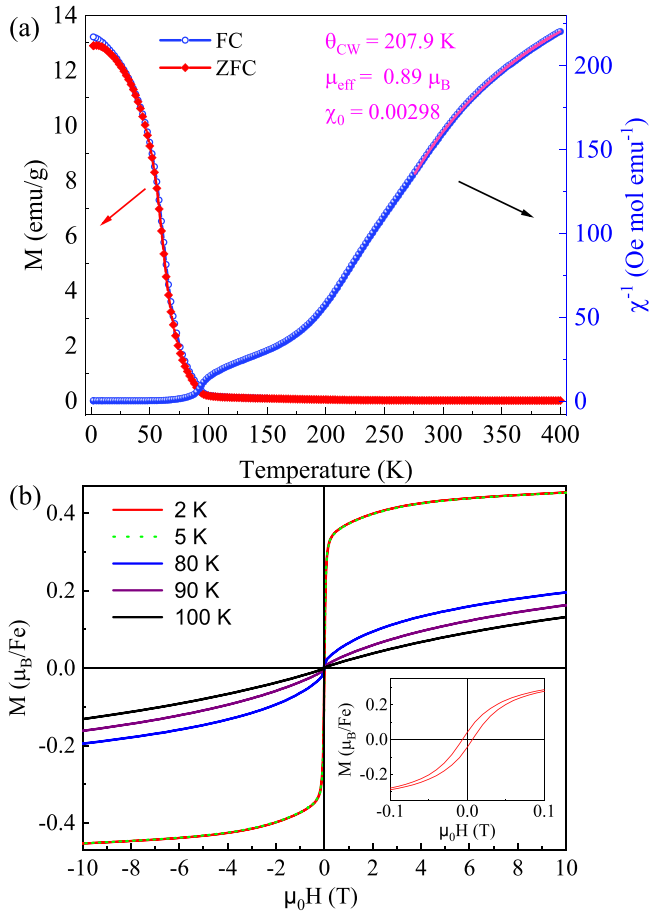

FIG. 3. (a) Temperature dependence of the magnetization, ZFC-FC $M(T)$ (left axis), and inverse susceptibility, $\chi^{-1}(T)$ (right axis), of $GeFe_3N$ measured with an external field of 0.1 T. (b) Isothermal magnetization measurements at various temperatures. The inset in (b) shows a magnified view of the hysteresis loop around zero field at 2 K. The complex $\chi^{-1}(T)$ curve above T_c, where appropriate Curie-Weiss fit cannot be made, indicates the breakdown of the Curie-Weiss behavior. However, a tentative fit of the data in the high-temperature range was made only to compare with other works.

the Curie-Weiss theory

$$\chi(T) = \chi_0 + \frac{C}{T - \theta_{CW}}, \tag{1}$$

where χ_0 is a temperature-independent term that may arise from core diamagnetism (either from the sample or from the sample holder), Pauli paramagnetism, or van Vleck paramagnetism [23], $C = N\mu_{\text{eff}}^2/(3k_B)$ is the Curie constant, θ_{CW} is the Weiss temperature, k_B is the Boltzmann constant, and μ_{eff} is the effective magnetic moment per Fe atom. The fitted results are $\chi_0 = 2.98 \times 10^{-3}$ emu Oe^{-1} mol^{-1}, $\theta_{\text{CW}} = 207.9$ K, and $\mu_{\text{eff}} = 0.89\ \mu_B$. The positive value of θ_{CW} is consistent with the FM-like correlation, as mentioned above. However, the fitted effective magnetic moment is much smaller than the spin-only moment of Fe atoms in typical magnetic materials. This is consistent with earlier reported results of mixing local and itinerant magnetism in $GeFe_3N$ for the two Fe sites [18]. We also estimate the saturation magnetic moment by using the law of approach to saturation method to the $M(H)$ curve

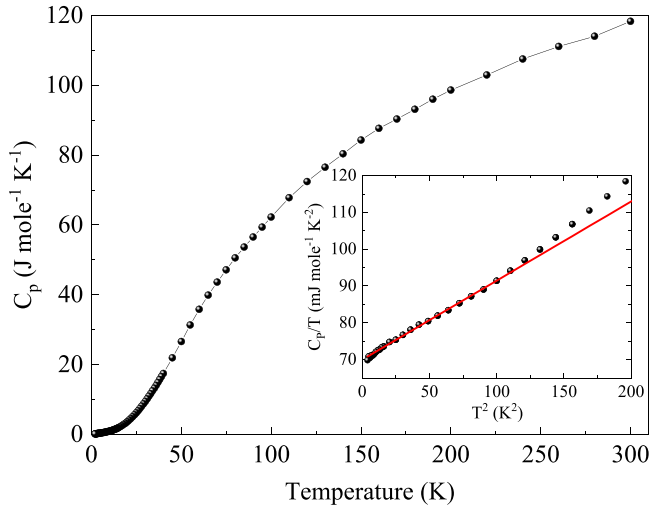

FIG. 4. Specific heat $C_P(T)$ of $GeFe_3N$ as a function of temperature measured under zero external magnetic field. The inset shows the C_P/T vs T^2 plot of the low-temperature part of the $C_P(T)$ data. The solid line through the data point in the inset is a fit (see the text for details) in the temperature range of 1.8–10 K.

at 2 K. At high external magnetic fields, the $M(H)$ data can be expressed as [24]

$$M(H) = M_S(1 - a/H - b/H^2) + kH, \tag{2}$$

where M_S, a, b, and k are fitting parameters. The determined $M_S = 0.45\ \mu_B$/Fe is even smaller than the effective magnetic moment obtained from the Curie-Weiss fits and the DFT calculated values [18]. In principle, antiferromagnetic alignment between the spins at FeI and FeII sites, which leads to a ferrimagnetic order, can explain the above observed small value of M_S. However, this is inconsistent with the strong FM correlation between FeI and FeII sites obtained from our DFT calculations. Therefore, these results are also consistent with the short-range FM order in $GeFe_3N$, which is in line with the ZFC-FC magnetic measurements shown in Fig. 3(a).

C. Specific heat

To reveal the short-range nature of the FM order as suggested in our magnetic measurements, we show the zero-field specific heat $C_P(T)$ data of $GeFe_3N$ in Fig. 4. No obvious anomalies were found in the entire temperature range. This is inconsistent with the λ-shape peak at the transition temperature corresponding to the sudden release of the magnetic entropy as expected for usual magnetic transitions. Therefore, our specific heat data also suggests a short-range ordered FM ground state in $GeFe_3N$.

In the inset of Fig. 4, we show the C_P/T vs T^2 plot of the low-temperature part of the $C_P(T)$ data. The Debye function $C_{ph} \sim \beta_3 T^3$ together with the electronic specific heat $C_{el} \sim \gamma T$ were used to fit the $C_P(T)$ data in the low-temperature range (1.8–10 K). The best fitting gives $\beta_3 = 2.116\,98 \times 10^{-4}\ \text{J K}^{-4}\ \text{mol}^{-1}$ and $\gamma = 70.1\ \text{mJ K}^{-2}\ \text{mol}^{-1}$, respectively. The large electronic specific heat suggests a large effective electron mass renormalization, likely by the spin fluctuations of the short-range FM order, which puts the studied

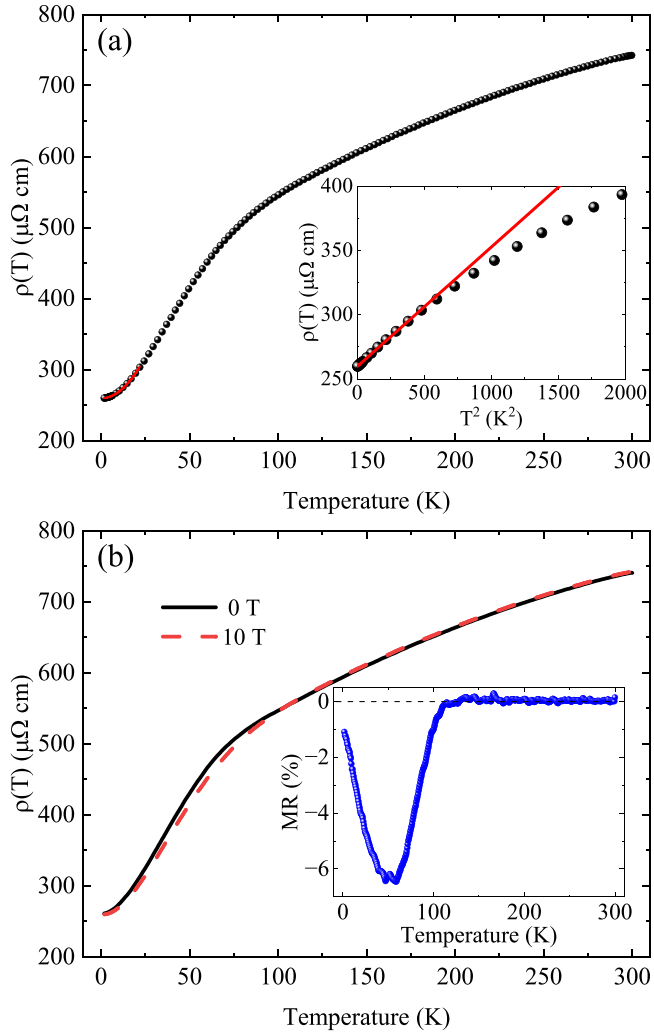

FIG. 5. (a) Resistivity as a function of temperature measured in zero magnetic field and (b) comparison of the resistivity measured in zero field and in 10 T magnetic field. Inset in (a) shows the $\rho(T)$ vs T^2 plot of the zero-field resistivity data. Solid lines through the data point at the low-temperature range are theoretical fits by the expression $\rho(T) = \rho_0 + aT^2$. Inset in (b) shows the magnetoresistivity $[\mathrm{MR}(T) = [\rho_H(T) - \rho_0(T)]/\rho_0(T)]$ at 10 T.

$GeFe_3N$ as a heavy-fermion (HF) system. The HF state is usually observed in the f-electron compounds with localized f-spins [25]; however, it was also observed in 3d electron systems, such as the first observed 3d HF compound LiV_2O_4 [26,27], the iron-based high-temperature superconductors (K, Rb, Cs)Fe_2As_2 [28], and the recently found room temperature van der Waals ferromagnet family Fe_3(Ga, Ge)Te_2 [29–31]. We believe that the interesting HF behavior of $GeFe_3N$ is highly related to the coexistence of local and itinerant magnetism, which is similar to that of the Fe_3GaTe_2 [29] ferromagnet.

D. Resistivity

To further study the short-range FM-like transition, we made resistivity measurements under zero magnetic field and under 10 T magnetic field as shown in Figs. 5(a) and 5(b). One can see that both the zero-field and 10-T-field resistivities decrease with decreasing temperature, indicating the metallic nature of our sample, which is similar to that of the $ZnFe_3N$ and $AlFe_3N$ compounds [14] and is consistent with DFT calculations [18]. Near $T_c \sim 95$ K, both $\rho(T)$ curves show a clear cross-over-like behavior signaling the onset of the short-range FM-like order, which is consistent with the dc magnetization data shown in Fig. 3(a). Below about 25 K, the low-temperature resistivity follows the usual T^2 temperature dependence. These results, together with the enhanced electronic specific heat γ, are characteristics of HF behavior, with emergent Fermi-liquid (FL) behavior being similar to that observed in other 3d HF compounds [26–31]. Theoretical fitting with $\rho(T) = \rho_0 + aT^2$ leads to $a = 0.09295\ \mu\Omega\,\mathrm{cm\,K^{-2}}$ and a high residual resistivity $\rho_0 = 259.6\ \mu\Omega\,\mathrm{cm}$. The residual resistivity ratio amounts to $\mathrm{RRR} = \rho(300\ \mathrm{K})/\rho_0 = 2.86$. The high residual resistivity and low RRR value might be due to the polycrystalline nature and possible defects in our sample. With increasing temperature, the resistivity gradually deviates from the FL behavior and shows a linear temperature dependence around 50 K where a negative valley of the magnetoresistivity $[\mathrm{MR}(T) = [\rho_H(T) - \rho_0(T)]/\rho_0(T)]$ can be seen from the inset of Fig. 5(b). The observed small negative MR suggests a suppression of the spin-disorder scatterings by the applied external magnetic field, which is consistent with the observed short-range FM-like order.

E. AC susceptibility

The lack of long-range order and possible disorders associated with nitrogen vacancies in the sample may lead to glassy behavior as reported earlier by Kan *et al.* [17] in their sample. Therefore, we further performed ac susceptibility measurements on our $GeFe_3N$ sample. In Figs. 6(a) and 6(b), we present the temperature dependence of the real $\chi'(T)$ and imaginary $\chi''(T)$ parts of the ac susceptibility measured at indicated frequencies under zero dc bias field, respectively. With decreasing temperature, a small hump appears immediately below the FM-like transition temperature, $T_c \sim 95$ K, which is consistent with the dc magnetic measurements shown in Fig. 3(a). With further decreasing temperature, both $\chi'(T)$ and $\chi''(T)$ curves exhibit clear peaks at around 57.5 K [see the enlarged view in the inset of Fig. 6(a)]. In addition to the main peak, the $\chi''(T)$ curves exhibit a shoulder-like irregularity near 40 K and a small dip near 30 K, which might be a memory effect due to the glassy nature [32] of our sample. However, the peak position for our $GeFe_3N$ sample is about ~17 K higher than the value of ~40.5 K reported by Kan *et al.* [17], which could be attributed tentatively to chemical differences due to different sample preparations. Interestingly, the peak position determined from the $\chi'(T)$ curve depends only weakly on the measurement frequency, as shown in the inset in Fig. 6(b). Together with the weak bifurcation effect appears between the ZFC and FC curves as shown in Fig. 3(a), these results might suggests a weak spin-glass behavior similar to that reported by Kan *et al.* [17] for their $GeFe_3N$ sample. On the other hand, our observation is a little different with that observed by Kan *et al.* [17] and other conventional spin-glass systems [33–36]. The observed small changes of the peak position with increasing frequency suggest a much faster spin

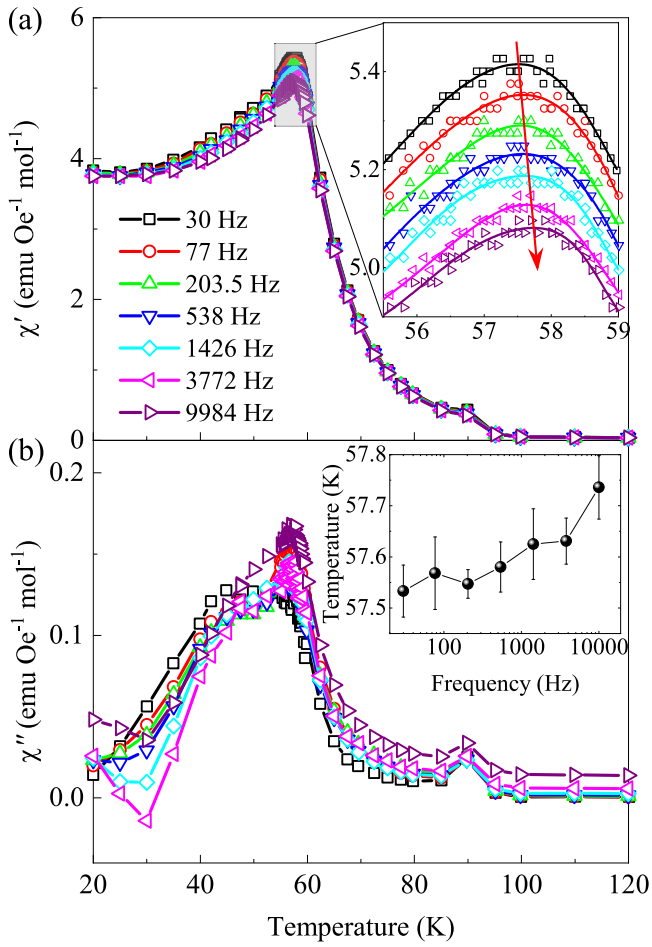

FIG. 6. AC susceptibility data: (a) temperature dependence of the real part of the ac susceptibility χ', measured at various frequencies and under zero dc bias field. (b) The imaginary part of the corresponding ac susceptibility χ''. Inset in (a) shows the enlarged part around the peak position of the real part of the ac susceptibility χ'. Inset in (b) shows the frequency dependency of the peak positions extracted from the $\chi'(T)$ data.

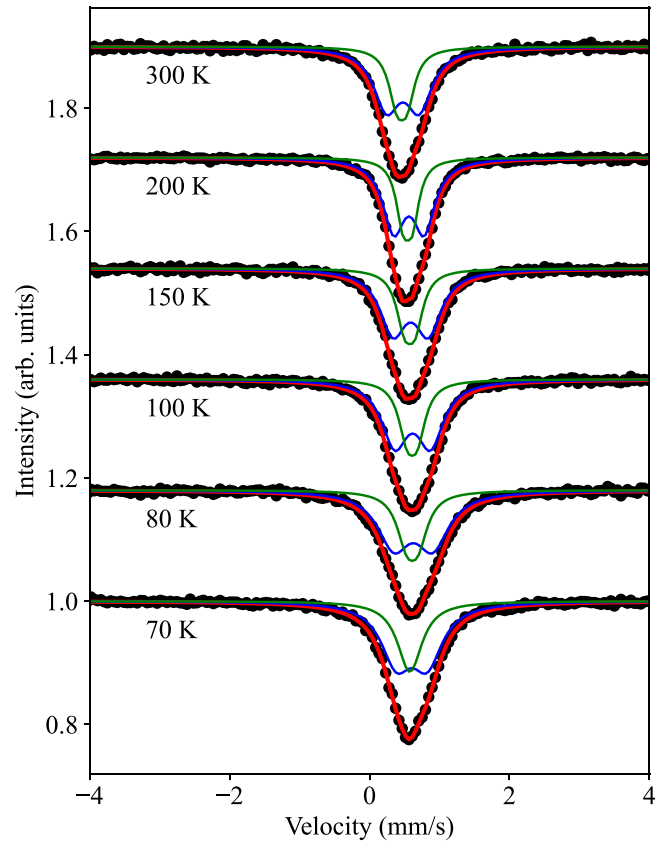

FIG. 7. ^{57}Fe Mössbauer spectra (black dots) of the $GeFe_3N$ samples measured in the temperature range of 70–300 K. Solid lines are fits to the experimental data with two doublets as described in the text.

relaxation process than that of the conventional spin-glass systems. This interesting behavior might be rooted in the strong interplay between the local and itinerant magnetism of the two crystallographic Fe sites in the $GeFe_3N$ [17,18].

F. Mössbauer spectroscopy

There are two nonequivalent local crystallographic sites for the Fe atoms in the $GeFe_3N$ crystal structure. Earlier experiments [17] and DFT calculations [18] have shown that the Fe atoms at the two different sites exhibit local and itinerant magnetism with calculated (PBE functional) magnetic moment of $\mu_{\mathrm{FeI}} = 1.72\,\mu_B$ and $\mu_{\mathrm{FeII}} = 0.30\,\mu_B$, respectively. To investigate the properties of the two Fe sites separately, we performed ^{57}Fe Mössbauer spectroscopy measurements.

The Mössbauer spectra taken in the temperature range of 70–300 K are shown in Fig. 7. At 300 K, the spectrum can be well reproduced by superimposing two subspectrum with an intensity ratio of 1:2 corresponding to the Fe atoms siting at FeI and FeII sites, respectively. With decreasing temperature, we observed an increase of the spectral line width below ∼100 K. This is consistent with the $T_c = 95$ K determined from our magnetization measurements. However, no sextet subspectrum corresponding to the FM state can be resolved above ∼60 K. This means that the hyperfine magnetic fields for both Fe sites are too small to be resolved from the two doublets, indicating that only very short-range FM correlations are established at this stage. Therefore, the spectra collected in this temperature range were fitted with only two doublets, as shown in Fig. 7.

In Fig. 8, we present the Mössbauer spectra measured in the temperature range of 5–60 K. For these spectra, a sextet corresponding to the FeI site with larger local moments can be resolved in addition to the two doublets. In principle, there should be another sextet corresponding to the FeII site with smaller itinerant moments. However, our trial fits failed, even at the lowest measured temperature of 5 K, due to the small hyperfine field value and the strong overlap with the two doublets. Therefore, we fitted our spectra with only one sextet and two doublets as shown in Fig. 8. One can see that the sextet makes only a minor contribution (∼11.5% at 5 K) to the total spectrum while the major contributions are still the two paramagnetic doublets. This is clear evidence that the PM-FM phase transition is never completed even at the lowest measured temperature of 5 K. This means that the sample is

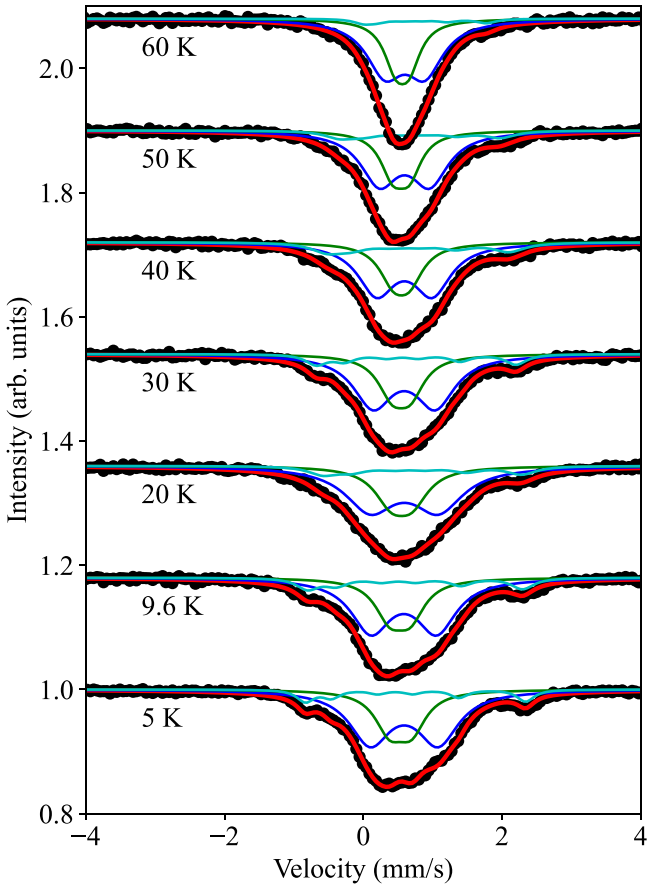

FIG. 8. ^{57}Fe Mössbauer spectra (black dots) of the $GeFe_3N$ samples measured in the temperature range of 5–60 K. Solid lines are fits to the experimental data with two doublets and one sextet as described in the text.

composed of FM clusters embedded in the PM background, which is consistent with the short-range FM ground state suggested from our magnetic and specific heat measurements.

There might be some site inversion between the Ge and Fe sites as observed by Burghaus *et al.* in their $Ga_{0.9}Fe_{3.1}N$ sample [37], which might be due to the considerable Ga deficiencies in their sample. However, we believe that this is not the case for our sample, since the composition of our sample is close to the nominal one and we did not observe any additional subspectrum that corresponds to the ^{57}Fe ions at the Ge site in our high-temperature Mössbauer measurements (see Fig. 7). Moreover, the above-observed sextet in our low-temperature Mössbauer spectra has a much smaller hyperfine field, ∼10 T, when compared to the huge hyperfine field, ∼28 T, as observed for the ^{57}Fe ions at the Ga site forming the Fe_{13} metallic clusters [37]. Therefore, the sextet observed in our low-temperature Mössbauer spectra should come from the ^{57}Fe ions at the FeI site in the short-range FM regions.

The deduced hyperfine parameters as a function of temperature are shown in Fig. 9. Above the FM transition temperature T_c, the isomer shifts exhibit similar values for

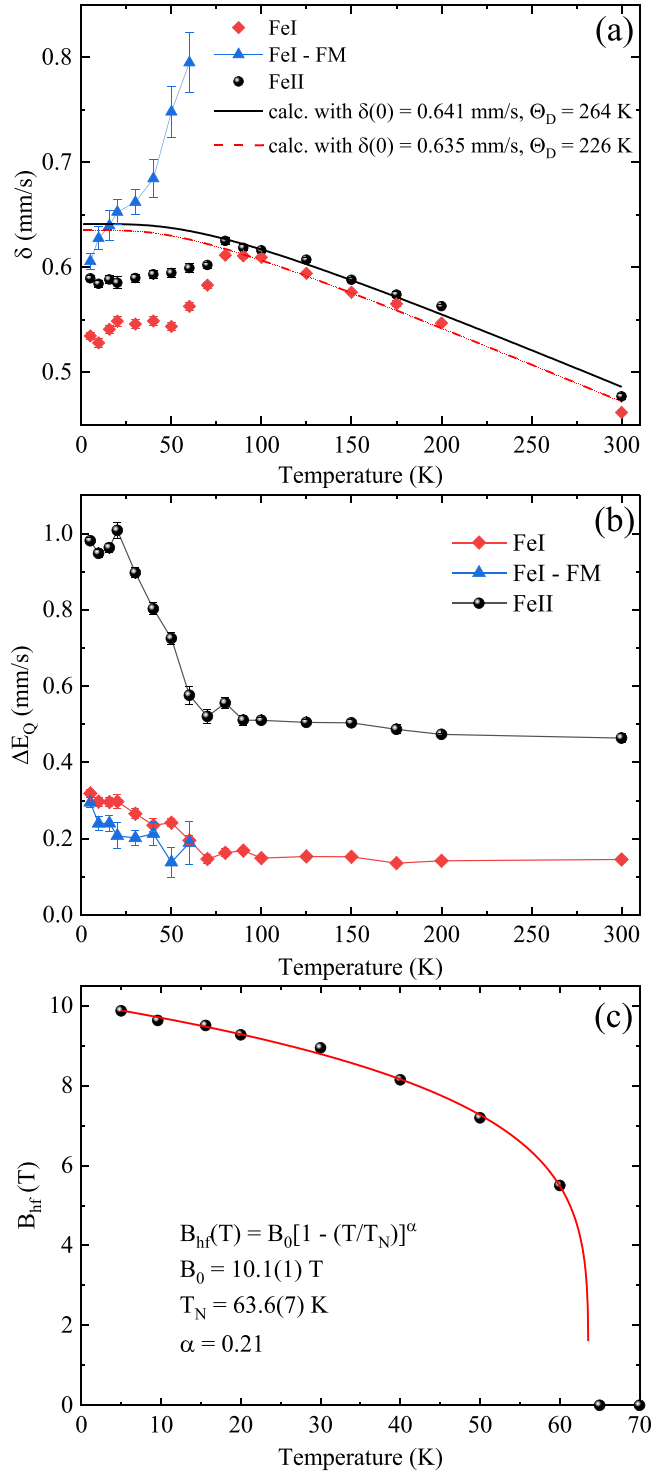

FIG. 9. Hyperfine parameters of (a) isomer shift $\delta(T)$, (b) quadruple splitting $\Delta E_Q(T) = \frac{1}{2}eQ|V_{zz}|(1+\eta^2/3)^{1/2}$, and (c) hyperfine magnetic field $B_{hf}(T)$ deduced from the fits of the Mössbauer spectra shown in Figs. 7 and 8. Solid lines in (a) are calculated theoretical curves according to the Debye model with indicated parameters. Solid lines in (b) are guides to the eye. Solid line in (c) is theoretical fit to the experimental data using the usual power-law relation, $B_{hf}(T) = B_{hf}(0)[1-(T/T_N)]^{\alpha}$.

both FeI and FeII sites. With decreasing temperature, they both increase following the Debye model for the second-order Doppler shift [38],

$$\delta(T) = \delta(0) - \frac{9}{2}\frac{k_B T}{Mc}\left(\frac{T}{\Theta_D}\right)^3 \int_0^{\Theta_D/T} \frac{x^3 dx}{e^x - 1}, \qquad (3)$$

where $\delta(0)$ is the temperature-independent chemical shift, and the second part is the temperature-dependent second-order Doppler shift. k_B is the Boltzmann constant, M is the mass of the Mössbauer nucleus, c is the speed of light, and Θ_D is the Debye temperature. The solid lines in Fig. 9(a) are calculated theoretical curves with zero temperature isomer shifts of $\delta(0)_{\mathrm{FeI}} = 0.635\,\mathrm{mm/s}$, $\delta(0)_{\mathrm{FeII}} = 0.641\,\mathrm{mm/s}$ and Debye temperatures of $\Theta_D(\mathrm{FeI}) = 226\,\mathrm{K}$ and $\Theta_D(\mathrm{FeII}) = 264\,\mathrm{K}$. Below T_c, clear anomalies deviating from the Debye model can be seen for both sites, suggesting the changes of the s-electron densities at the Fe nuclei. For the quadruple splittings $\Delta E_Q = \frac{1}{2}eQ|V_{zz}|(1+\eta^2/3)^{1/2}$ shown in Fig. 9(b), they are almost constant with decreasing temperature for both sites at higher temperature ranges. Below T_c, the quadruple splittings increase clearly with decreasing temperature for both sites, indicating changes of the distribution symmetry of the charges around the Fe nuclei [39].

The temperature-dependent hyperfine magnetic fields $B_{hf}(T)$, deduced from the fits of the Mössbauer spectra shown in Fig. 8, are shown in Fig. 9(c). We have employed the empirical formula $B_{hf}(T) = B_0[1-(T/T_N)]^{\alpha}$ to fit the data. The fitted results are $B_{hf}(0) = 10.1(1)\,\mathrm{T}$ and $T_N = 63.6\,\mathrm{K}$. The resulted critical exponent is $\alpha = 0.21$, which is much smaller than the expected three-dimensional (3D) Heisenberg critical exponent of 0.36 [40,41]. Instead, the value is rather close to the theoretical value of 0.23 for the two-dimensional (2D) XY model [42,43], which might be due to the stacking of the FeI layer with local spins and the FeII layer with itinerant spins along the c axis.

III. DFT CALCULATIONS

To understand the above experimental results, DFT calculations were performed. First, we have used the CASTEP *ab initio* simulation code [44] for the structural optimization starting from the refined experimental lattice parameters. For the exchange correlation functional, generalized gradient approximation (GGA) with the PBE [45] parametrization was used. The pseudopotential files were generated on the fly by the CASTEP code using atomic configurations of Ge $3d^{10}4s^24p^2$, N $2s^22p^3$, and Fe $3d^64s^2$. The kinetic energy cutoff of the plane wave basis was set to 489.805 eV by setting the basis precision level to fine. Brillouin zone integration was sampled using a Γ-centered [46] k mesh of $8\times8\times6$. The total energies were converged to less than $10^{-8}\,\mathrm{eV/atom}$ to achieve good self-consistency in the electronic step. The Broyden-Fletcher-Goldfarb-Shanno (BFGS) variant of the quasi-Newton optimization method [47] was used and the positions of the ions were relaxed toward the equilibrium position until the force acting on each atom was less than $10^{-2}\,\mathrm{eV/Å}$.

The relaxed structural parameters are listed in Table I, and the optimized lattice constants are found to be $a = 5.21126\,\mathrm{Å}$ and $c = 7.74688\,\mathrm{Å}$, which is close to the value of $a = 5.2133\,\mathrm{Å}$ and $c = 7.7638\,\mathrm{Å}$ found by using the full potential all-electron code WIEN2K with PBE functional [18]. The calculated magnetic moments are $M_{\mathrm{FeI}} = 1.78\,\mu_B$ and $M_{\mathrm{FeII}} = 0.263\,\mu_B$ for FeI and FeII sites, respectively. These values are close to previous calculated values of $M_{\mathrm{FeI}} = 1.72\,\mu_B$ and $M_{\mathrm{FeII}} = 0.30\,\mu_B$ [18] and are consistent with our Mössbauer spectroscopy results, where only the hyperfine field at the FeI site can be determined, whereas the hyperfine field at the FeII site is too small to be resolved.

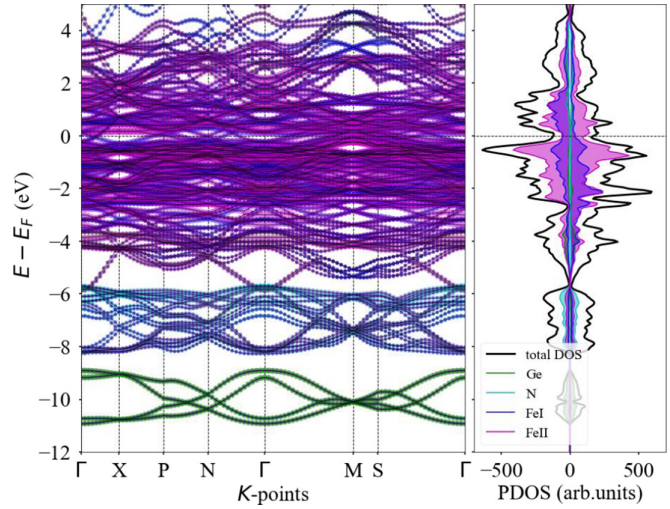

FIG. 10. Calculated band structure and PDOS of $GeFe_3N$.

For the density of states (DOS) and band-structure calculations, we have used the full potential linearized augmented plane wave (FP-LAPW) method as implemented in the ELK code [48]. Same as in the structural relaxation, GGA approximation with the PBE [45] exchange-correlation functional was used. The plane-wave cutoff was set to $R_{\mathrm{MT}} \times |\mathbf{G}+k|_{\mathrm{max}} = 7.0$ Hartree and the maximum $\mathbf{G}$ vector for the potential and density was set to $|\mathbf{G}|_{\mathrm{max}} = 12.0$ Hartree. The Γ-centered k-point mesh of $8\times8\times6$ was used. The muffin-tin radii R_{MT} were set to 2.400 a.u., 1.513 a.u., and 2.017 a.u. for Ge, N, and Fe atoms, respectively. The total energy and Kohn-Sham potential were converged to less than 0.0272 meV and 2.72×10^{-4} meV, respectively. The effect of spin orbital coupling (SOC) was found to be small on the band structure and, therefore, it was neglected in the following discussion. The calculated spin moments are found to be $M_{\mathrm{FeI}} = 1.71\,\mu_B$ and $M_{\mathrm{FeII}} = 0.32\,\mu_B$, being close to the values obtained by the CASTEP and WIEN2K code [18].

The calculated band structure and partial density of states (PDOS) of $GeFe_3N$ are shown in Fig. 10, which were decomposed into characteristics of individual elements. We have found that the bands in the energy range of $-11\sim-9\,\mathrm{eV}$ are mainly from Ge s-electrons with negligible contributions from the Fe d-electrons. In the energy range of $-8\sim-6\,\mathrm{eV}$, the bands are composed of N p-electrons and Fe d-electrons. The broader bands near the Fermi level are mainly from the Fe d-electrons with minor contributions from the Ge and N p-electrons. As pointed out in earlier works [18,49], it is interesting to find considerable hybridization between the two Fe sites. Therefore, significant exchange interaction may be expected between the two Fe sites, which should be important

TABLE II. The calculated Heisenberg isotropic exchange parameters $J_{ij}^{\rm iso}$ of bulk $GeFe_3N$ for the first seven pairs as indicated in Fig. 1, where N_S is the coordination number.

J_N	J_{ij} (meV)	Distance (Å)	Type	N_S
J_1	-0.6421	2.679	FeII-FeII	4
J_2	4.8656	2.709	FeI-FeII	8
J_3	-0.0587	2.805	FeII-FeII	1
J_4	4.2426	3.685	FeI-FeI	4
J_5	0.1356	3.789	FeII-FeII	2
J_6	6.8476	3.873	FeI-FeI	2
J_7	0.1491	3.972	FeII-FeII	2

to understanding the interesting magnetic behavior observed in our experiments.

To analyze the magnetic interactions in $GeFe_3N$, we adopt the following Heisenberg Hamiltonian [50]:

$$E = -\sum_{i\neq j}\left[J_{ij}^{\rm iso}\vec{S}_i\cdot\vec{S}_j + \vec{S}_i J_{ij}^{\rm ani}\vec{S}_j + \vec{D}_{ij}\cdot(\vec{S}_i\times\vec{S}_j)\right] - \sum_i A_i(\vec{S}_i\cdot\vec{r}_i)^2, \quad (4)$$

where the first term is the isotropic exchange, the second term is the symmetric anisotropic exchange with $J_{ij}^{\rm ani}$ being a 3×3 symmetric tensor, the third term is the antisymmetric Dzyaloshinskii-Moriya (DM) interaction, and the final term represents the single-ion anisotropy (SIA). First, we determine the SIA by comparing the energies of $GeFe_3N$ with the spin axis pointing along different directions with SOC included in the calculations. It was found that $GeFe_3N$ shows an easy-plane anisotropy with an energy of 0.63 eV/Fe lower when the spins are pointing within the *ab* plane than along the *c* axis. This is consistent with the critical exponent of $\alpha = 0.21$ found in our Mössbauer experiments, which is close to the value of 0.23 for the 2D XY model.

Next, the interatomic Heisenberg exchange parameters have been calculated using the TB2J package [50] interfaced to the atomic-orbital based *ab initio* computation at USTC (ABACUS) DFT code [51,52]. The DFT part calculation with ABACUS was done by considering collinear ferromagnetic ground states including the SOC effect. The basis set of linear combination of atomic orbitals (LCAO) was used with an energy cutoff of 1361 eV. The optimized norm-conserving Vanderbilt pseudopotentials [53,54] (version 2.0.1) were used to calculate the Hamiltonian and overlap matrix with Γ-centered *k*-point mesh of $9\times 9\times 6$. Then, the exchange parameters were calculated straightforwardly by using the TB2J code with a *k*-mesh of $7\times 7\times 5$. As shown in Fig. 11, the calculated anisotropic exchange $J_{ij}^{\rm ani}$ and DM interaction D are about two orders of magnitude smaller than the isotropic exchange $J_{ij}^{\rm iso}$, as expected for $GeFe_3N$ with negligible SOC effect. The calculated first seven pairs of the isotropic exchange parameters $J_{ij}^{\rm iso}$ are listed in Table II. Clearly, the interactions for the FeII-FeII pair type are all one order of magnitude smaller than the others. Interestingly, on the other hand, the interactions for the FeI-FeII pair type are as strong as those for the FeI-FeI pair type interactions. These results clearly indicate the strong interplay between the local spins at the FeI site and the itinerant spins at the FeII site. Therefore, the strong exchange interactions between the local FeI spins tend to order at higher temperatures while the weak interactions between the itinerant FeII spins tend to order at lower temperatures, and the strong interplay between them may introduce frustration that leads to the observed short-range ordered FM ground state as observed in our experiments.

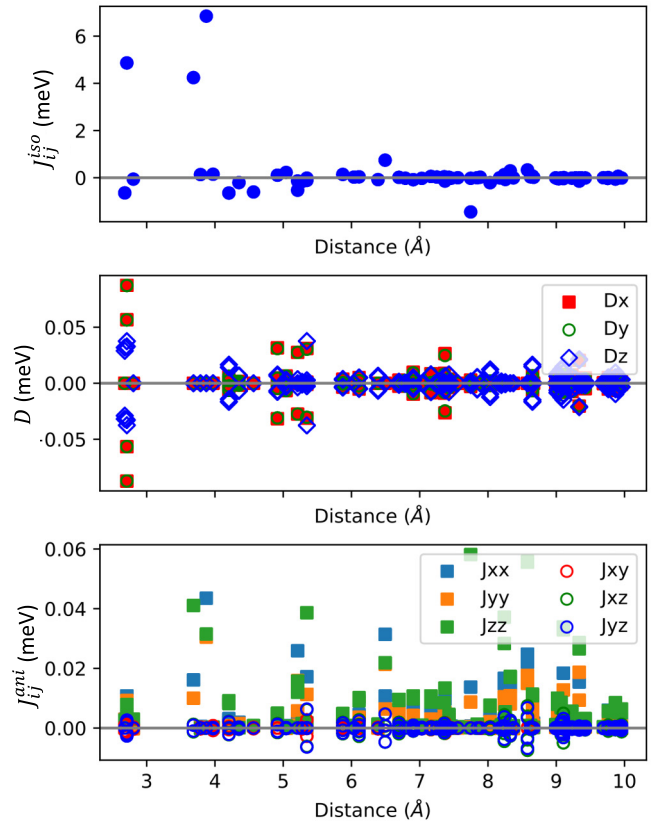

FIG. 11. The calculated exchange parameters (a) isotropic exchange $J_{ij}^{\rm iso}$, (b) DM interaction D, and (c) the anisotropic exchange $J_{ij}^{\rm ani}$ for $GeFe_3N$ from TB2J-ABACUS.

Finally, to better understand the FM transition induced changes of the electron distribution at the Fe nuclei, we present the difference in electron density distribution between the FM and NM states ($n_{\rm diff} = n_{\rm FM} - n_{\rm NM}$) of the $GeFe_3N$ in Fig. 12. There is no obvious difference in the electron density distribution at the Ge and N sites as expected from the nonmagnetic nature of these two atoms. Interestingly, the changes in the electron density distribution at both FeI and FeII sites have the character of 3*d* orbitals, which is consistent with our band character analysis. To be precise, at the FeI site, the in-plane d_{xy} electrons decrease and the out-of-plane d_{xz}, d_{yz}, and d_{z^2} electrons increase upon entering the FM state from the NM state. For the FeII site, the in-plane $d_{x^2-y^2}$ electrons decrease and the out-of-plane $d_{yz} \pm d_{xz}$ electrons increase. The increased electron density in the *z* direction will lead to more negative V_{zz} values [38]. Considering the negative V_{zz} values of $V_{zz}({\rm FeI}) = -1.27\times 10^{21}$ V/m^2 and $V_{zz}({\rm FeII}) = -3.53\times 10^{21}$ V/m^2 from our CASTEP calculation [55,56], a more negative V_{zz} will give an increase of

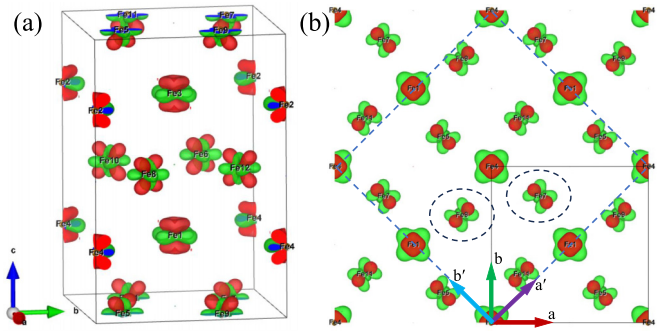

FIG. 12. The difference in electron density distribution between the FM and NM states ($n_{\text{diff}} = n_{\text{FM}} - n_{\text{NM}}$) of the $GeFe_3N$ shown in (a) side view and (b) top view (only two layers are shown) of the 3D isosurface. The red and green color represent positive and negative values of n_{diff}, respectively. As labeled in (a) and (b), atoms from Fe1 to Fe4 are at the FeI site and Fe5–Fe12 are at the FeII site. Shown in (b) are two choices of different unit cells that rotated 45° with respect to each other as described in the text in order to reveal the orbital order for the FeII layer. The Fe atom labeled as Fe7 (Fe9), as circled in (b), has a higher orbital occupation of the $d_{yz} - d_{xz}$ ($d_{yz} + d_{xz}$) orbitals in the conventional coordinate system or the $d_{y'z'}$ ($d_{x'z'}$) orbitals in the rotated $a'b'c'$ coordinate system.

the quadruple splitting $\Delta E_Q(T) = \frac{1}{2}eQ|V_{zz}|(1+\eta^2/3)^{1/2}$ as observed in Fig. 9(b).

More interestingly, as shown in Fig. 12(b), there might be an orbital order in the FeII layer. The Fe atom labeled with Fe7 (Fe9), as circled in Fig. 12(b), has a higher orbital occupation of the $d_{yz} - d_{xz}$ ($d_{yz} + d_{xz}$) orbitals in the conventional coordinate system (labeled with *abc*). To quantify the orbital occupation, we made Mulliken population analysis in a rotated bigger unit cell as shown in Fig. 12(b) with the CASTEP code. The orbital occupations of the 3*d* orbitals are listed in Table III. Clearly, the orbital occupation of the $d_{z'^2}$, $d_{x'^2-y'^2}$, and $d_{x'y'}$ orbitals are almost the same for Fe7 and Fe9 atoms. On the other hand, the Fe7 atom has a higher orbital occupation of the $d_{y'z'}$ orbital compared to the $d_{x'z'}$ orbital, while the Fe9 atom shows the opposite orbital occupation for the two $d_{y'z'}/d_{x'z'}$ orbitals. The orbital ordering at the FeII site is interesting, however, verification in experiments could be difficult for the current system due to the weak orbital polarization and short-range nature of the FM state. Therefore, as a subject of future investigation, extremely sensitive experimental setups are definitely required for the successful detection of the orbital order in $GeFe_3N$.

TABLE III. The calculated orbital populations for the two atoms labeled with Fe7 and Fe9, as circled in Fig. 12(b). The orbital labels are shown in the rotated bigger unit cell $a'b'c'$ as shown in Fig. 12(b).

	Mulliken populations				
Atoms	$d_{z'^2}$	$d_{y'z'}$	$d_{x'z'}$	$d_{x'^2-y'^2}$	$d_{x'y'}$
Fe7	1.344	1.584	1.412	1.260	1.294
Fe9	1.341	1.417	1.584	1.253	1.291

IV. SUMMARY

In summary, we have performed comprehensive structural, magnetic, specific heat, resistivity, and Mössbauer spectroscopy measurements on a $GeFe_3N$ sample. The XRD refined structural parameters have confirmed the nitrogen stoichiometry and rotation of the FeII atoms away from the diagonal position. The magnetic, specific heat, and Mössbauer measurements have revealed a short-range ordered FM ground state. Our DFT calculations have shown the coexistence of local and itinerant magnetism in $GeFe_3N$ with local spins at the FeI site and itinerant spins at the FeII site. More importantly, the exchange interactions between the local spins at the FeI site and the itinerant spins at the FeII site are as strong as that between the local spins at the FeI site and much larger than the interactions between the itinerant spins at the FeII site. Moreover, our DFT calculations have shown that possible orbital order may exist at the FeII site, which deserves further investigation with sensitive experimental setups. These results are important for the understanding of the observed short-range FM ground state in $GeFe_3N$ and are also important for a better understanding of the complex relationships between the structure and magnetism in related materials.

ACKNOWLEDGMENTS

This paper was supported by the National Natural Science Foundation of China (Grant No. U23A20547), the National Key Research and Development Program of China (Grant No. 2022YFB4101401), and the Guangdong Basic and Applied Basic Research Foundation (Grant No. 2022B1515120020). The authors are grateful for the support provided by the Supercomputing Center of Lanzhou University.

[1] L. Néel, Magnetism and local molecular field, Science **174**, 985 (1971).
[2] J. Knolle and R. Moessner, A field guide to spin liquids, Annu. Rev. Condens. Matter Phys. **10**, 451 (2019).
[3] H. Yu, J. Xiao, and H. Schultheiss, Magnetic texture based magnonics, Phys. Rep. **905**, 1 (2021).
[4] J. M. D. Coey, Magnetism in d^0 oxides, Nat. Mater. **18**, 652 (2019).
[5] J M Santiago, C-L Huang, and E Morosan, Itinerant magnetic metals, J. Phys.: Condens. Matter **29**, 373002 (2017).
[6] S. Schmitt, N. Grewe, and T. Jabben, Itinerant and local-moment magnetism in strongly correlated electron systems, Phys. Rev. B **85**, 024404 (2012).
[7] P. Vilmercati, A. Fedorov, F. Bondino, F. Offi, G. Panaccione, P. Lacovig, L. Simonelli, Michael A. McGuire, Athena S. M. Sefat, D. Mandrus, Brian C. Sales, T. Egami, W. Ku, and N. Mannella, Itinerant electrons, local moments, and magnetic correlations in the pnictide superconductors $CeFeAsO_{1-x}F_x$ and $Sr(Fe_{1-x}Co_x)_2As_2$, Phys. Rev. B **85**, 220503(R) (2012).
[8] E. Fawcett, Spin-density-wave antiferromagnetism in chromium, Rev. Mod. Phys. **60**, 209 (1988).

[9] G. Grüner, The dynamics of spin-density waves, Rev. Mod. Phys. **66**, 1 (1994).

[10] G. Grüner, The dynamics of charge-density waves, Rev. Mod. Phys. **60**, 1129 (1988).

[11] T. Scholz and R. Dronskowski, Improved ammonolytic synthesis, structure determination, electronic structure, and magnetic properties of the solid solution $Sn_xFe_{4-x}N$ ($0 < x < 0.9$), Inorg. Chem. **54**, 8800 (2015).

[12] J. Burghaus, M. Wessel, A. Houben, and R. Dronskowski, Ternary nitride $GaFe_3N$: An experimental and quantum-theoretical study, Inorg. Chem. **49**, 10148 (2010).

[13] A. Houben, P. Müller, Jörg von Appen, H. Lueken, R. Niewa, and R. Dronskowski, Synthesis, crystal structure, and magnetic properties of the semihard itinerant ferromagnet $RhFe_3N$, Angew. Chem. Int. Ed. **44**, 7212 (2005).

[14] Y. Fu, S. Lin, and B. Wang, High-temperature soft magnetic properties of antiperovskite nitrides $ZnNFe_3$ and $AlNFe_3$, J. Magn. Magn. Mater. **378**, 54 (2015).

[15] A. M. Glazer, The classification of tilted octahedra in perovskites, Acta Crystallogr. Sect. B **28**, 3384 (1972).

[16] S. Iikubo, K. Kodama, K. Takenaka, H. Takagi, M. Takigawa, and S. Shamoto, Local lattice distortion in the giant negative thermal expansion material $Mn_3Cu_{1-x}Ge_xN$, Phys. Rev. Lett. **101**, 205901 (2008).

[17] X. C. Kan, B. S. Wang, L Zhang, L Zu, S Lin, J. C. Lin, P Tong, W. H. Song, and Y. P. Sun, Critical behavior in tetragonal antiperovskite $GeNFe_3$ with a frustrated ferromagnetic state, Phys. Chem. Chem. Phys. **19**, 13703 (2017).

[18] M. Tsumuraya and D. J. Singh, Violation of the rule of parsimony: Mixed local moment and itinerant Fe magnetism in Fe_3GeN, Phys. Rev. B **106**, 024408 (2022).

[19] K. Momma and F. Izumi, *VESTA3* for three-dimensional visualization of crystal, volumetric and morphology data, J. Appl. Crystallogr. **44**, 1272 (2011).

[20] The FullProf Suite, http://www.ill.eu/sites/fullprof/.

[21] Z. Klencsár, E. Kuzmann, and A. Vértes, User-friendly software for Mössbauer spectrum analysis, J. Radioanal. Nucl. Chem. **210**, 105 (1996).

[22] H Boller, Komplexcarbide und-nitride mit aufgefülltem U_3Si-typ, Monatshefte für Chemie **99**, 2444 (1968).

[23] S. Mugiraneza and A. M. Hallas, Tutorial: a beginner's guide to interpreting magnetic susceptibility data with the Curie-Weiss law, Commun. Phys. **5**, 95 (2022).

[24] H. Zhang, D. Zeng, and Z. Liu, The law of approach to saturation in ferromagnets originating from the magnetocrystalline anisotropy, J. Magn. Magn. Mater. **322**, 2375 (2010).

[25] G. R. Stewart, Heavy-fermion systems, Rev. Mod. Phys. **56**, 755 (1984).

[26] H. Takagi, C. Urano, S. Kondo, M. Nohara, Y. Ueda, T. Shiraki, and T. Okubo, Transport properties of metallic LiV_2O_4 single crystals-heavy mass Fermi liquid behavior, Mater. Sci. Eng. B **63**, 147 (1999).

[27] C. Urano, M. Nohara, S. Kondo, F. Sakai, H. Takagi, T. Shiraki, and T. Okubo, LiV_2O_4 spinel as a heavy-mass Fermi liquid: Anomalous transport and role of geometrical frustration, Phys. Rev. Lett. **85**, 1052 (2000).

[28] Y. P. Wu, D. Zhao, A. F. Wang, N. Z. Wang, Z. J. Xiang, X. G. Luo, T. Wu, and X. H. Chen, Emergent Kondo lattice behavior in iron-based superconductors AFe_2As_2 (A = K, Rb, Cs), Phys. Rev. Lett. **116**, 147001 (2016).

[29] Y. Zhang, H. Lu, X. Zhu, S. Tan, W. Feng, Q. Liu, W. Zhang, Q. Chen, Y. Liu, X. Luo, D. Xie, L. Luo, Z. Zhang, and X. Lai, Emergence of Kondo lattice behavior in a van der Waals itinerant ferromagnet, Fe_3GeTe_2, Sci. Adv. **4**, eaao6791 (2018).

[30] J.-X. Zhu, M. Janoschek, D. S. Chaves, J. C. Cezar, T. Durakiewicz, F. Ronning, Y. Sassa, M. Mansson, B. L. Scott, N. Wakeham, E. D. Bauer, and J. D. Thompson, Electronic correlation and magnetism in the ferromagnetic metal Fe_3GeTe_2, Phys. Rev. B **93**, 144404 (2016).

[31] B. Chen, J. Yang, H. Wang, M. Imai, H. Ohta, C. Michioka, K. Yoshimura, and M. Fang, Magnetic properties of layered itinerant electron ferromagnet Fe_3GeTe_2, J. Phys. Soc. Jpn. **82**, 124711 (2013).

[32] T. Jonsson, K. Jonason, P. Jönsson, and P. Nordblad, Nonequilibrium dynamics in a three-dimensional spin glass, Phys. Rev. B **59**, 8770 (1999).

[33] K. Gunnarsson, P. Svedlindh, P. Nordblad, L. Lundgren, H. Aruga, and A. Ito, Dynamics of an Ising spin-glass in the vicinity of the spin-glass temperature, Phys. Rev. Lett. **61**, 754 (1988).

[34] L. Sandlund, P. Granberg, L. Lundgren, P. Nordblad, P. Svedlindh, J. A. Cowen, and G. G. Kenning, Dynamics of Cu-Mn spin-glass films, Phys. Rev. B **40**, 869 (1989).

[35] S. Guchhait, G. G. Kenning, R. L. Orbach, and G. F. Rodriguez, Spin glass dynamics at the mesoscale, Phys. Rev. B **91**, 014434 (2015).

[36] S. Nayak, S. Ghorai, A. M. Padhan, S. Hajra, P. Svedlindh, and P. Murugavel, Cationic redistribution induced spin-glass and cluster-glass states in spinel ferrite, Phys. Rev. B **106**, 174402 (2022).

[37] J. Burghaus, M. T. Sougrati, A. Möchel, A. Houben, R. P. Hermann, and R. Dronskowski, Local ordering and magnetism in $Ga_{0.9}Fe_{3.1}N$, J. Solid State Chem. **184**, 2315 (2011).

[38] P. Gütlich, E. Bill, and A. X. Trautwein, *Mössbauer Spectroscopy and Transition Metal Chemistry* (Springer, Berlin, Heidelberg, 2011).

[39] Z. Li, Y. Fang, X. Ma, H. Pang, and F. Li, Charge redistribution at the antiferromagnetic phase transition in the SrFeAsF compound, Phys. Rev. B **84**, 134509 (2011).

[40] J. C. Le Guillou and J. Zinn-Justin, Critical exponents for the n-vector model in three dimensions from field theory, Phys. Rev. Lett. **39**, 95 (1977).

[41] J. C. Le Guillou and J. Zinn-Justin, Critical exponents from field theory, Phys. Rev. B **21**, 3976 (1980).

[42] A. Taroni, S. T. Bramwell, and P. C. W. Holdsworth, Universal window for two-dimensional critical exponents, J. Phys.: Condens. Matter **20**, 275233 (2008).

[43] U. Köbler and A. Hoser, Critical magnetic behaviour in one and two dimensions, J. Magn. Magn. Mater. **311**, 523 (2007).

[44] S. J. Clark, M. D. Segall, C. J. Pickard, P. J. Hasnip, M. J. Probert, K. Refson, and M. C. Payne, First principles methods using CASTEP, Z. Kristall. **220**, 567 (2005).

[45] J. P. Perdew, K. Burke, and M. Ernzerhof, Generalized gradient approximation made simple, Phys. Rev. Lett. **77**, 3865 (1996).

[46] H. J. Monkhorst and J. D. Pack, Special points for Brillouin-zone integrations, Phys. Rev. B **13**, 5188 (1976).

[47] B. G. Pfrommer, M. Cote, S. G. Louie, and M. L. Cohen, Relaxation of crystals with the quasi-Newton method, J. Comput. Phys. **131**, 233 (1997).

[48] The Elk Code, http://elk.sourceforge.net/.

[49] C. Liu, C. Zhang, X. Kan, X. Liu, S. Feng, Y. Yang, Q. Lv, J. Hu, and M. Shezad, Evolution of structural transformation in $\gamma - Fe_4N$ and $GeNFe_3$, J. Phys. Chem. C **124**, 6321 (2020).

[50] X. He, N. Helbig, M. J. Verstraete, and E. Bousquet, TB2J: A Python package for computing magnetic interaction parameters, Comput. Phys. Commun. **264**, 107938 (2021).

[51] P. Li, X. Liu, M. Chen, P. Lin, X. Ren, L. Lin, C. Yang, and L. He, Large-scale *ab initio* simulations based on systematically improvable atomic basis, Comput. Mater. Sci. **112**, 503 (2016).

[52] M. Chen, G-C Guo, and L. He, Systematically improvable optimized atomic basis sets for *ab initio* calculations, J. Phys.: Condens. Matter **22**, 445501 (2010).

[53] D. R. Hamann, Optimized norm-conserving Vanderbilt pseudopotentials, Phys. Rev. B **88**, 085117 (2013).

[54] D. R. Hamann, Erratum: Optimized norm-conserving Vanderbilt pseudopotentials [Phys. Rev. B **88**, 085117 (2013)], Phys. Rev. B **95**, 239906(E) (2017).

[55] M. Profeta, F. Mauri, and C. J. Pickard, Accurate first principles prediction of 170 NMR parameters in SiO_2: Assignment of the zeolite ferrierite spectrum, J. Am. Chem. Soc. **125**, 541 (2003).

[56] C. Bonhomme, C. Gervais, F. Babonneau, C. Coelho, F. Pourpoint, T. Azais, S. E. Ashbrook, J. M. Griffin, J. R. Yates, F. Mauri, and C. J. Pickard, First-principles calculation of NMR parameters using the gauge including projector augmented wave method: A chemist's point of view, Chem. Rev. **112**, 5733 (2012).